



HAL
open science

Sustainable Route for Nd Recycling from Waste Electronic Components Featured with Unique Element-Specific Sorting Enabling Simplified Hydrometallurgy

Dong Xia, Nicolas Charpentier, Ange Maurice, Andrea Brambilla, Qingyu Yan, Jean-Christophe P. Gabriel

► **To cite this version:**

Dong Xia, Nicolas Charpentier, Ange Maurice, Andrea Brambilla, Qingyu Yan, et al.. Sustainable Route for Nd Recycling from Waste Electronic Components Featured with Unique Element-Specific Sorting Enabling Simplified Hydrometallurgy. Chemical Engineering Journal, 2022, 441, pp.135886. 10.1016/j.cej.2022.135886 . cea-03621104

HAL Id: cea-03621104

<https://cea.hal.science/cea-03621104>

Submitted on 22 Jul 2024

HAL is a multi-disciplinary open access archive for the deposit and dissemination of scientific research documents, whether they are published or not. The documents may come from teaching and research institutions in France or abroad, or from public or private research centers.

L'archive ouverte pluridisciplinaire **HAL**, est destinée au dépôt et à la diffusion de documents scientifiques de niveau recherche, publiés ou non, émanant des établissements d'enseignement et de recherche français ou étrangers, des laboratoires publics ou privés.



Distributed under a Creative Commons Attribution - NonCommercial 4.0 International License

1 Sustainable Route for Nd Recycling from Waste Electronic Components

2 Featured with Unique Element-Specific Sorting Enabling Simplified

3 Hydrometallurgy

4 Dong Xia^{a,*}, Nicolas M. Charpentier^a, Ange A. Maurice^a, Andrea Brambilla^b, Qingyu Yan^a, Jean-
5 Christophe P. Gabriel^{a,c,*}

6 ^a SCARCE Laboratory, Energy research institute @ NTU, Nanyang Technological University, 50 Nanyang
7 Drive, 639798, Singapore

8 ^b Université Grenoble Alpes, CEA Leti, 38054 Grenoble, France

9 ^c Université Paris-Saclay, CEA, CNRS, NIMBE, LICSEN 91191, Gif-sur-Yvette, France

10

11 * Corresponding authors

12 E-mail addresses: xiadong@ntu.edu.sg (D. Xia), jean.gabriel@cea.fr (J-C. P. Gabriel)

13 Abstract:

14 Neodymium being an expensive strategic metal indispensable for our society, the key issue is to secure
15 its supply and make its usage sustainable. However, with less than 1% of it currently being recycled,
16 we are far from achieving this. Although some work is underway to recycle electrical engines' large
17 Nd-based magnet alloys, little attention has been given to recycling small Nd-containing ceramic-based
18 components, despite their 12% share of the Nd market. Herein, we demonstrate an economically viable
19 Nd recycling process from such components found in electronic wastes. We tackled the issue of high
20 Nd dilution in complex e-wastes through the upstream deployment of simultaneous disassembly,
21 machine vision and multi-energy X-ray transmission sorting (first-of-its-kind), followed by precise
22 beneficiation in virtue of the difference in magnetism, density and fracture toughness. The resulting
23 concentrates are mainly dielectric ceramics (BaO-Nd₂O₃-TiO₂), containing 38.3% of Nd. Although
24 ceramics are refractory in general, Nd can be simply leached in concentrated HNO₃ from these

1 dielectrics with high selectivity under optimized conditions. Subsequently, Nd can be recovered by
2 oxalate precipitation while 60% of HNO₃ can be regenerated. To elaborate on the mechanism of the
3 leaching, the related kinetics, thermodynamics and bonding nature were investigated through theoretical
4 computations. The overall Nd recovery efficiency reaches 91.1% ending up with commercial-grade
5 Nd₂O₃ (> 99.6%). More importantly, the recycling route is estimated profitable within four years based
6 on conservative margins. This work provides a promising strategy to recover rarely recycled strategic
7 metals towards a closed-loop design.

8 *Keywords:*

9 Neodymium sustainability

10 Ceramic capacitor

11 Multi-energy X-ray transmittance (ME-XRT)

12 Precise beneficiation

13 Selective leaching

14 Integrated recycling route

15

16

17

18

19

1 **1. Introduction**

2 Rare earth elements (REEs) play a vital role in revolutionizing modern technologies involving
3 communications, electrical vehicles, renewable energy, state-of-the-art materials and other applications
4 that impact our daily life [1-4]. Although not being scarce in geological terms, REEs have gained global
5 attention as strategic resources due to the uneven regional distribution of economically viable ores, and
6 concerns about scarcity in supply chains [5-7]. The global market for REEs is estimated at 221 thousand
7 tons for the year 2020, which is essential to industries worth trillions of dollars [8]. Among the 17 REEs,
8 Nd is acknowledged as one of the most critical in terms of its importance to clean energy production
9 and its supply chain associated risks [9], and demand is anticipated to rise by 700% from 2010 to 2035
10 [10]. In response to tightened Chinese export quotas, many countries have gathered pace in diversifying
11 their supply chains [11].

12 Given the technical difficulties in mining and separation, and the associated adverse environmental
13 consequences, a few countries, like the U.S., are boosting their REE production from primary resources,
14 while other countries that lack REE resources, like Europe and Japan, are gearing up REE recycling
15 from secondary resources [12,13]. This is particularly beneficial if the recycled REEs are those that are
16 in short supply [14,15]. Therefore, some research has been seen in recent years of recycling Nd from
17 end-of-life permanent magnets and rechargeable batteries, with a focus on utilizing chemical routes
18 (Table S1) [16-20]. The recycling potential is obvious, but substantial chemical use and effluent
19 treatment inhibits a profitable industry. Other endeavours were devoted to resolving the high variability
20 of input materials [21,22], or targeting green REE production and recycling, such as bioleaching [23,24],
21 peptide-based mineralization [25], selective crystallization [26], selective absorption through
22 nanoengineered cellulose [27] and selective ligand chemistry based on thermodynamic or kinetic

1 control [28,29]. Nevertheless, the current recycling rate of Nd is still extremely low (~1% in Europe)
2 due to the challenge to economical integrating of the new processes into existing processes [30].
3 Certainly, sustainable Nd recycling routes are urgently required to achieve a circular Nd economy.

4 Beyond magnets and batteries, there is also an important potential, yet ignored, for recycling Nd
5 from ceramic-based electronic components, which accounts for 12 % of total Nd end uses [31].
6 Ceramics that contain Nd are a family of microwave dielectric materials commonly used in mobile
7 phones, base stations and other electronic and communication applications [32]. With the arrival of the
8 5G era and the trend of electronic miniaturization, the applications of these ceramics will increase
9 astronomically due to their excellent dielectric properties [33,34]. Unlike recycling of large magnets or
10 battery alloys which have easier access to their resources, these waste dielectrics are discarded with a
11 deluge of highly complex e-wastes, in which Nd is so diluted that it is at trace concentrations. Despite
12 existing industrial processes that dismantle e-wastes, pre-concentration of Nd from individual
13 components is far more challenging to achieve because element-specific sorting technology does not
14 exist [35,36]. Indeed, sensor-based sorting has found industrial applications [37], but they are not
15 element-specific (except for laser induced breakdown spectroscopy, but this spectroscopy can only
16 perform near surface analysis) [38]. X-ray imaging may provide elemental identification because the
17 concomitant photon energies span the spectroscopic features of most elements, but little actual
18 application to e-waste processing has yet been established beyond single or dual energy transmission
19 [39]. Hence our hypothesis that, despite the challenges, an integrated technical innovation able to fully
20 exploit selectivity, based on optical, X-ray spectroscopy and other physico-mechanical methods, should
21 provide enough Nd pre-concentration to make Nd recycling possible.

22 In this article, we therefore report the first economically viable integrated route to recycle Nd from

1 waste printed circuit boards (PCBs), enabling us to achieve both a high recovery rate and high product
2 purity. The route consists of simultaneous disassembly of electronic components (ECs); advanced
3 sorting of these ECs; precise beneficiation to pulverise some materials, and then selective
4 hydrometallurgy to separate the chemical elements (Fig 1). Furthermore, it obeys a material closed-loop
5 design, exploiting maximum mechanophysical advantage and requiring minimum chemical input and
6 process steps.

7 **2. Materials and methods**

8 *2.1. Materials*

9 E-wastes were collected from Vans Chemistry Pte. Ltd., in India and Metalo international Pte. Ltd.,
10 in Singapore. The obtained e-wastes included PCBs, computers, mobile phones, televisions and other
11 small household appliances (Fig. S1a). These complete electronic and electrical devices were first
12 subject to manual disassembly to retrieve their PCBs (Fig. S1b). All the PCBs were heated in a box
13 furnace (lindberg/Blue M, Thermo Scientific) at ~250 °C for 10 mins to melt solder and were shaken
14 to release the surface-mounted ECs (Fig. S1c). These ECs were then mingled as the original e-waste
15 stream for the sorting study. In addition, single layer ceramic capacitors (SLCCs, COG/NP0 Dielectric)
16 were procured from Vishay Intertechnology, Inc. to supplement the source of Nd-containing ECs for
17 the study of the subsequent beneficiation and hydrometallurgy processes. Neodymium (III) nitrate
18 hexahydrate (99.9%), neodymium oxide (99.9%), nitric acid (AR, 70%), hydrochloric acid (AR, 37%),
19 sulphuric acid (AR, 95-98%), oxalic acid dihydrate (AR, ≥ 99%), sodium hydroxide (AR, ≥ 97%) and
20 oxalate standard (TraceCERT®) were purchased from Sigma-Aldrich. Metal standard solutions,
21 including neodymium, barium, titanium, silver, copper and tin were purchased from PerkinElmer. Ultra-
22 pure water was obtained from a water purification system (WaterPro®, Labconco Co.) with a resistivity

1 of 18.2 M Ω -cm at 25 °C. All of the chemicals were used as received.

2 2.2. *Optical sorting of ECs*

3 To specifically target ceramic capacitors using optical sorting, we narrowed the size range of ECs
4 by selecting two categories, 1-5 mm and 5-10 mm, for the sieved samples. The optical sorting of these
5 ECs was performed on a self-designed conveyor belt prototype (2.5 m long and 10 cm wide) integrated
6 with a vibratory bowl feeder (Fig. S2a). The ECs were continuously conveyed on the belt at a speed of
7 0.9 m/s and passed through a filming zone, where images of the ECs were captured by an industrial
8 camera (12 mm fixed focal lens, 25 images per second, BU505MCF Telicam, Toshiba) lit by a white
9 LED ring (V2DR-i90A-W, Vital Vision Technology). The images were then processed with machine
10 vision techniques to identify the distinctive traits of the various ECs, such as colours, appearances,
11 edges and sizes. Specifically, a convolutional neural network (CNN) was applied to classify the traits
12 that were stored in the database. The CNN was written in Python (version 3.6.8) using an open-source
13 library (TensorFlow) and was built on a sequential mode based on three 2D convolution blocks with a
14 max pool layer corresponding to each convolution layer. Finally, electro-pneumatic nozzles diverted the
15 recognized ECs off the belt into sorting bins by directional airflow. Recovery rate and sorting accuracy
16 were specified as the evaluation index for the sorting performance with the following equations:

$$17 \text{ Recovery rate (\%)} = \frac{\text{the amount of sorted target ECs}}{\text{the input amount of target ECs}} \times 100\% \quad (1)$$

$$18 \text{ Sorting accuracy (\%)} = \frac{\text{the amount of sorted target ECs}}{\text{the amount of ECs in the target bin}} \times 100\% \quad (2)$$

19 2.3. *ME-XRT sorting of SLCCs*

20 The element-based identification of SLCCs was performed on a modular fashioned ME-XRT
21 device (Fig. S2b). X-ray was generated from an Yxlon source operating at 120 kV and 1.2 mA, with 1
22 mm aluminium filtration. The XRT spectrum were recorded by a multi-energy X-ray detector (ME100,

1 Detection Technology) with an acquisition time of 100 ms for each line, composed of 128 pixels,
2 corresponding to the physical pixels of the detector. The SLCC samples were placed on cardboard that
3 was attached to a motorized stage travelling at 0.4 cm/s along a direction perpendicular to both the
4 detector line and the X-ray beam. The source was placed at 150 cm from the detector and 100 cm from
5 the sample. The XRT mapping over the entire scanning area was acquired by integrating the total
6 transmittance of each pixel on a full energy range (20-150 keV). The XRT spectrum of each individual
7 SLCC was simply averaged from all the pixels that compose the SLCC body area to remove the photon
8 signal noise from the detector. The K-edges of elements can be interpreted from the XRT spectrum. The
9 performance of ME-XRT sorting was simulated with a Python code by considering both the K-edge
10 distinctiveness of various elements and the ejection accuracy of the conveyor belt. The ME-XRT sorting
11 is currently being implemented onto our sorting conveyor, and is awaiting X-ray device operation
12 licensing.

13 *2.4. Physical beneficiation of Nd concentrates*

14 The physical beneficiation process was composed of several consecutive processing units as shown
15 in Fig. S3. The sorted Nd-containing SLCCs were coarsely shredded by a cutting mill (1 mm built-in
16 sieve, SM200, Retsch) to liberate inner materials from cladding epoxy resins. Afterwards,
17 ferromagnetic particles, which were mainly from connecting wires, were separated by means of a
18 permanent magnet. Non-magnetic materials were transferred into a 1 L measuring cylinder that was
19 half-full of tap water and were stirred intermittently until the particles were stratified according to their
20 different settling velocities. Then the epoxy resin fraction was elutriated out with tap water from the top
21 layer. The remaining heavy fraction was transferred to a mortar and was subject to brittle fracturing. As
22 ceramics are brittle and metals are generally more ductile, we could readily comminute the dielectric

1 fraction into finer powder while the metal fraction was flattened. Finally, Nd-containing dielectric
2 fraction was obtained from the powder passing through a 0.25 mm sieve.

3 *2.5. Acidic leaching of Nd*

4 The remaining metal impurities were first removed through preferential leaching, which was
5 processed with a pulp density of 1500 g/L in 10 M HNO₃ at 25 °C for 5 min. After filtration and drying,
6 the resulting solid phase was used as actual dielectric material (DM) for Nd leaching. The leaching was
7 carried out in a 100 mL round bottom flask connected with a reflux condenser to minimize the loss of
8 acid due to evaporation. A Teflon magnetic stirrer and weighted DM was loaded into the flask, which
9 was submerged into an oil bath. The leaching was performed while charging a known amount of acid.
10 The temperature was regulated by a hot plate (VWS-C7, VWR) and the stirring speed was maintained
11 at 500 rpm. 10 M HNO₃, 10 M HCl and 5 M H₂SO₄ were compared using the same leaching conditions
12 (50 g/L and 70 °C) to select the mineral acid that possessed the best leaching selectivity. Furthermore,
13 for the leaching with HNO₃, we applied a Box-Behnken response surface design (Design-Expert 12) to
14 study the effect of acid concentration, temperature and pulp density on the leaching rate, Nd
15 concentration at equilibrium, and leaching efficiency. The range of acid concentration (7.5-12.5 M) and
16 temperature (70-110 °C) were selected according to a correlation between HNO₃ boiling point and its
17 concentration, which was generated from EquilWin software (version 4.01). The pulp density was
18 studied in an industrially practical range (50-400 g/L). The maximization of the three responses and the
19 reasonability of each operating parameter were all considered to optimize the leaching condition (Table
20 S2). To follow the leaching kinetics, the leachate was withdrawn at different time intervals and the Nd
21 concentration was measured with XRF (calibrated by ICP-OES) until it reached a plateau. Moreover,
22 we also performed the leaching with samples withdrawn only at the plateau time to characterize the

1 final leachate solution and the solid residues after filtration (0.22 μm).

2 2.6. Precipitation and calcination

3 Nd precipitation experiments with oxalic acid were guided by specification simulations using
4 Hydra-Medusa software to optimize the Nd feed concentration and oxalic acid dosage. The precipitation
5 experiments were carried out in enclosed vials at 25 °C for 3 h with constant stirring. The concentrations
6 of Nd and oxalate (ox) ions were determined before and after precipitation. The precipitate after
7 filtration (0.22 μm) was calcined in a box furnace at 900 °C for 1 h to produce the final metal oxide
8 products.

9 2.7. Calculations in hydrometallurgy

10 The leaching kinetic data was fitted using the shrinking core models. The models under surface
11 chemical control (eq. 3) and product layer diffusion control (eq. 4) are respectively presented as [40]:

$$12 \quad 1 - (1 - x)^{1/3} = k_c \cdot t \quad (3)$$

$$13 \quad 1 - (2/3) x - (1 - x)^{2/3} = k_d \cdot t \quad (4)$$

14 where k_c and k_d represent the apparent chemical reaction rate constant (h^{-1}) and the apparent diffusion
15 reaction rate constant (h^{-1}), respectively. x is the time-dependent fraction at time t (h) and is expressed
16 as:

$$17 \quad x = M_t / M_0 \times 100\% \quad (5)$$

18 where M_0 is the initial mass of Nd in DM and M_t is the instantaneous mass of Nd in the leachate.

19 The leaching efficiency (x_{LE}) and precipitation efficiency (x_{PR}) were calculated with the following
20 equations:

$$21 \quad x_{LE} = M_L / M_0 \times 100\% \quad (6)$$

$$22 \quad x_{PR} = (1 - M_P / M_L) \times 100\% \quad (7)$$

1 where M_L is the mass of ion in leachate and M_P is the mass of ion in the solution after precipitation.

2 According to the Arrhenius equation, the relationship between the specific rate constant k (k_c or k_d)
3 and the absolute temperature (T , K) can be correlated, thus the apparent activation energy E_a ($\text{kJ}\cdot\text{mol}^{-1}$)
4 can be estimated by taking the natural logarithm of the Arrhenius equation:

$$5 \ln k = \frac{-E_a}{R} \left(\frac{1}{T} \right) + \ln A \quad (8)$$

6 where A is the frequency factor, and R is the universal gas constant ($8.3145 \text{ J}\cdot\text{K}^{-1}\cdot\text{mol}^{-1}$).

7 Using Outotec HSC Chemistry software (v 9.5.1), standard enthalpy of formation (ΔH_f^0 , $\text{kJ}\cdot\text{mol}^{-1}$)
8 and standard Gibbs free energies of formation (ΔG_f^0 , $\text{kJ}\cdot\text{mol}^{-1}$) at certain temperatures were obtained
9 from the database or the estimation module for reactants and products involved in reactions. Therefore,
10 the thermodynamic data of the reactions, including Gibbs free energies ($\Delta_r G^0$, $\text{kJ}\cdot\text{mol}^{-1}$), enthalpy
11 change ($\Delta_r H^0$, $\text{kJ}\cdot\text{mol}^{-1}$) and entropy change ($\Delta_r S^0$, $\text{kJ}\cdot\text{mol}^{-1}\cdot\text{K}^{-1}$), can be calculated according to Hess'
12 law.

13 2.8. Sample characterizations

14 Metal contents in raw SLCC samples and calcined products were measured with an ICP–OES (OP
15 Optima 8000, PerkinElmer) after acidic digestion at $240 \text{ }^\circ\text{C}$ for 1.5 h using a microwave digestion
16 system (ETHOS UP, MILESTONE). Metal concentrations in solution were measured after required
17 dilution using either an ICP-OES or a handheld XRF spectrometer (Vanta C series, Olympus) calibrated
18 by the ICP-OES. The pH of the solution was measured by an analytical pH meter (SevenCompact,
19 METTLER TOLEDO) after dilution of 20000 times considering that the dissociation of highly diluted
20 HNO_3 is almost complete [41]. Concentrations of oxalate ions in solution were analysed with ion
21 chromatography (930 Compact IC Flex, Metrohm). Phase compositions of samples were examined by
22 a powder X-ray diffractometer (XRD-6000, Shimadzu) with $\text{Cu K}\alpha$ ($\lambda=1.5406 \text{ \AA}$) radiation, employing

1 a step size of 0.01° , in a range of $10 \leq 2\theta \leq 80$. The phase quantities were calculated by the elemental
2 composition or were analysed by MAUD software (v 2.98) on a basis of Rietveld refinement. Surface
3 morphology and elemental mapping of solid phase was characterized by scanning electron microscopy
4 equipped with energy dispersive X-ray spectroscopy (SEM-EDS, JSM 7600F, JEOL). Microscopic
5 images were captured with a digital microscope ($\times 50$, RS Pro). Density of particles was measured with
6 water displacement method. To test fracture toughness of the DM, bulk SLCCs were hot mounted in
7 epoxy material in a cylindrical shape and ground with sandpaper to expose a polished surface of the
8 DM. The test was performed by a micro Vickers hardness tester (Wilson VH1150, Buehler) at a force
9 of 49 N with the peak load maintained for 10 s and the fracture toughness (K_c , $\text{MPa}\cdot\text{m}^{1/2}$) was calculated
10 following the equation [42]:

$$11 \quad K_c = \xi_V^R (E/H)^{1/2} (P/C_0^{3/2}) \quad (9)$$

12 where ξ_V^R is a material-independent constant of 0.016 ± 0.004 , E is Young's modulus (GPa), H is the
13 Vickers hardness ($H = P/2a^2$, GPa), P is the peak load (N), c is the characteristic dimensions of the radial
14 crack (m), and a is half of the diagonal length of indentation (m).

15 2.9. First-principles computations

16 Defect formation energies were computed based on density functional theory (DFT). The BaO-
17 Nd_2O_3 - TiO_2 system is known to construct from perovskite-like units, interrelated on the base of
18 tetragonal tungsten-bronze-structure, which can be represented as a connection of the following layers:
19 $(\text{Ba}_{1/2}\text{O})$ - $(\text{Ba}_{1/2}\text{TiO}_3)$ - (NdTiO_3) - (NdTiO_3) , thus this material tends to cleave along the $(\text{Ba}_{1/2}\text{O})$ plane
20 [43]. To simplify the computing process, we only selected BaTi_2O_5 and $\text{Nd}_2\text{Ti}_4\text{O}_{11}$ as approximate
21 representatives to compare the difference of defect formation energies between Ba and Nd. The First-
22 principles calculations of the unit cells were performed using Cambridge serial total energy package

1 (CASTEP)1 code, in which a plane wave basis set was used [44]. The Ba/Nd vacancy model was
2 obtained by removing Ba/Nd atoms from the corresponding unit cell. The exchange and correlation
3 interactions were modelled using the generalized gradient approximation (GGA) and the Perdew-
4 Burke-Ernzerhof (PBE)2 functional [45]. The Vanderbilt ultrasoft pseudopotential3 was used with a
5 cut-off energy of 500 Ev [46]. Geometric convergence tolerances were set at a maximum force of 0.03
6 eV/A°, maximum energy change of 10⁻⁵ eV/atom, maximum displacement of 0.001 A° and maximum
7 stress of 0.5 GPa. The sampling in the Brillouin zone was set at 3×3×3 with the Monkhorst-Pack method.

8 The formula to calculate the defect formation energy (E_F) is given by the following equation [47]:

$$9 \quad E_F = E_{\text{def}} - E_{\text{per}} - \mu_i \quad (10)$$

10 where E_{def} and E_{per} are total energies of defect and perfect unit cells, respectively. μ_i is the chemical
11 potential of the atom of element (Ba or Nd).

12 2.10. Flowsheet simulation and economic analysis

13 The flowsheet simulation and economic analysis were performed with SuperPro Designer software
14 (v 8.5) for the entire Nd recycling process based on a commercial scale. Since the upstream sorting and
15 beneficiation section can be operated in a continuous mode while the downstream hydrometallurgy
16 section was designed in a batch mode, we simulated the two sub-processes separately. The mass and
17 energy balance was calculated according to the same operating parameters optimized from lab-scale
18 experiments. The economic indices were estimated by taking into account fixed capital costs, operating
19 costs and revenues from major products. The price of each input and output material was defined based
20 on the built-in database of SuperPro Designer or the information from commercial websites. We used
21 a 1.0 w% fraction of Nd based ceramic capacitors for a general mix of electronic components obtained
22 from the disassembly of PCBs. This is based on our mass balance of the disassembly of 100 kg of PCBs
23 that contained ~10% of ceramic-based capacitors, of which the probability that these are Nd based
24 ceramics is 0.1. By focusing only on the Nd, without considering the recovery of other metals that are
25 known to be economically viable, we have defined an extremely conservative scenario. Besides, the
26 operating cost of the optical-x-ray sorting process could be as low as 0.2-0.3 \$/MT of the processed
27 material [48], while we set 2.8 \$/MT for utilities costs and 72.4 \$/MT for labour costs.

1 3. Results and Discussion

2 The first step of the process was a complete dismantling of waste PCBs, followed by a size sorting
3 using a sieving tower. Since many such processes already exist in industry (a field we recently reviewed)
4 [36], we did not investigate it further and just performed dismantling ourselves as per the description
5 given in Section 2.1.

6 3.1. Optical and ME-XRT sorting

7 The next step was to investigate sorting Nd-based ECs out of miscellaneous waste ECs. We worked
8 on two size ranges of waste ECs bins, 1-5 mm and 5-10 mm, in which single layer ceramic capacitors
9 (SLCCs), multiple layer ceramic capacitors (MLCCs), electrolytic capacitors, integrated circuits (ICs),
10 connectors, inductors, resistors and other surface-mount devices (SMDs) were present. These ECs were
11 continuously fed onto a homebuilt sorting prototype (1-10 kg/h capacity) equipped with a conveyer belt,
12 where their visual traits (colour, shape, edge and size) were captured and were subject to image analysis
13 with the aid of machine vision techniques (Fig. 2a). The ECs were classified according to the traits
14 stored in our database and were ejected pneumatically into different sorting bins. The average recovery
15 rate and sorting accuracy in a single iteration could reach 81.6% and 79.5%, respectively (Fig. 2b, c and
16 Fig. S4). However, in the case of SLCCs, recovery rates as high as 100%, with an average sorting
17 accuracy of 90.8%, were obtained owing to their distinctive visual trait (Fig. S5). The limitation of this
18 step was that it did not separate the capacitors as a function of their elemental composition.

19 Next, we acquired energy-resolved imaging of the resulting SLCCs by multi-energy XRT (ME-
20 XRT) scanning using a 64-energy-channel semiconductor photon-counting detector technology (Fig.
21 2d) [49]. With this technology, not only can we (i) separate SLCCs based on their transmittance, thus
22 discriminating between the average composition of heavier and lighter atoms, see prominent colourful

1 contrasts in Fig. 2e and XRF verification in Fig. S6; but for the first time in such sorting we were also
2 able to (ii) use each pixel's ME-XRT spectrum to separate components based on their element-specific
3 K-edge absorption analysis. The local minimum intensity of the ME-XRT spectral curve was found to
4 be located within a given range of the energy corresponding to the elemental K-edge, enabling us to
5 differentiate Nd from Ba and Ta (Fig. 2f). It's worth noting that although Ba is a constituted element
6 for both Ba-(Ca)-Ti-O and Ba-Nd-Ti-O SLCCs, their detected K-edges were found at 37.4 keV and
7 43.6 keV, respectively, indicating a proper sorting window between the two types of SLCCs. From this
8 data, and assuming the same ejection performance as in the optical sorting, we could estimate that ME-
9 XRT based sorting would enable an Nd based SLCC recovery rate of 100%. We measured that the final
10 (optical+ME-XRT) sorting bin, containing solely Nd ceramic based capacitors, would have a 15.1 wt.%
11 of Nd (hence worth ~\$25k/metric ton in its 99%+ pure oxide form).

12 *3.2. Precise beneficiation*

13 The sorted Nd-containing SLCCs were found to have distinctive three-layer structures (metallic-
14 ceramic-metallic) covered by epoxy resin as a protective coating (Fig. S7), and Nd was only present in
15 the innermost dielectric material (DM) (Fig. S8). To isolate the DM layer and allow for a pre-
16 concentration in Nd, the SLCCs were subjected to a series of physical beneficiation treatments. The
17 mass fraction of each composition following the processing flow is shown in Fig. 3a. After the liberation
18 of inner materials by coarse shredding, some ferromagnetic materials (FM) containing Fe and Ni were
19 removed by magnetic separation. Subsequently, the protective coating fraction was separated from the
20 dielectric and conductive materials (D&CM) through elutriation in water, taking advantage of the
21 difference in settling velocity, which, in the case of the same particle size, is proportional to the density
22 difference between particles and water, according to Stokes' Law (Fig. S9). The fracture toughness of

1 the DM was tested to be $1.92 \pm 0.28 \text{ MPa}\cdot\text{m}^{1/2}$ by indentation at a force of $\sim 50 \text{ N}$ (Fig. S10), implying
2 that the brittleness of the DM is similar to other well-known ceramics [42]. We therefore readily
3 separated the brittle DM from the ductile conductive material (CM) through brittle fracturing and
4 subsequent sieving in virtue of their different deformation/fracture responses to impression. The
5 retrieved ceramic rich DM fraction accounted for 36.5% of the total input mass.

6 Through the physical beneficiation, we were able to enrich the Nd content from 15.1% in the initial
7 SLCCs to 38.3% in the final Nd concentrate with the high Nd recovery rate of 92.8 % (Fig. 3b). The
8 XRD on the DM fraction showed a composition of $\text{Ba}_{3.6}\text{Nd}_{9.6}\text{Ti}_{18}\text{O}_{54}$ (50.2%), $\text{Nd}_2\text{Ti}_2\text{O}_7$ (27.3%), and
9 $\text{Nd}_4\text{Ti}_9\text{O}_{24}$ (7.8%), with some amorphous organic impurities accounting for the remainder (Fig. S11).
10 Actually, typical $\text{BaO-Nd}_2\text{O}_3\text{-TiO}_2$ based ceramics with a general formula of $\text{Ba}_{6-3n}\text{Nd}_{8+2n}\text{Ti}_{18}\text{O}_{54}$ have
11 a similar XRD pattern. The number n was endowed 0.8 due to the presence of $\text{Nd}_4\text{Ti}_9\text{O}_{24}$ when the
12 ceramic is rich in Nd_2O_3 [50]. Furthermore, the fractions of FM and CM, which account for 18.2% and
13 3.2% of the total input mass, respectively, were found to contain concentrated valuable metals such as
14 Cu and Sn, hence available for further resource recovery (Fig. S12).

15 3.3. Selective hydrometallurgy

16 Then, the DM fraction was subjected to a short course of initial leaching with 10 M HNO_3 for 5
17 min. As shown in Fig. S10, 98.2 % Ag and 93.4 % Cu were preferentially removed into the leachate,
18 while 99.9% of the Nd was retained in the solid phase. Sn also mostly remained in the solid phase as it
19 could form insoluble metastannic acid (H_2SnO_3). We then compared the leaching performance of three
20 mineral acids (Fig. 4a). HCl and HNO_3 demonstrated a similar leaching efficiency for Nd and Ba, higher
21 than that of H_2SO_4 . However, HNO_3 possessed better selectivity than HCl as there was much less
22 transfer of Ti into the leachate. Therefore, HNO_3 was selected as the best mineral acid to leach DM. An

1 additional study of the effects of operating parameters on the Nd leaching performance was performed,
2 based on a Box-Behnken response surface experimental design (Table S3 and Fig. S14). The results
3 indicated that raising the temperature significantly improved the reaction rate but slightly affected the
4 Nd leaching efficiency. Nd concentration at equilibrium increased almost linearly with pulp density in
5 the studied range. HNO₃ concentration did not directly influence the three responses; however, it can
6 affect the boiling point of HNO₃ (Fig. S15), which limits the maximum heating temperature at ambient
7 pressure. As a result, the optimal leaching condition was determined to be at 10 M HNO₃, 110 °C and
8 400 g/L. These optimal conditions provided the advantage of a better leaching selectivity for Nd over
9 Ba (Fig. S16). We also studied the kinetics of Nd leaching from the DM (Fig. S17). The kinetic data fit
10 better with Eq. (3), ($r^2 = 0.9966$, $n = 15$) than Eq. (4) ($r^2 = 0.9098$, $n = 15$) (see Section 2.7), indicating
11 that surface chemical control dominated the leaching kinetics instead of product layer diffusion control,
12 according to shrinking core models [40,51]. Under these determined optimal conditions, the leaching
13 equilibrium was reached within 25 hours, with final neodymium concentrations reaching close to 1 M,
14 and an Nd leaching efficiency of up to 99.3% (Fig. 4b).

15 After the leaching, the original smooth morphology of the DM particles was replaced by hundreds
16 of corrosion fronts and newly formed agglomerations of crystals, which varied in size from nano-scale
17 to sub-micro-scale depending on the duration of leaching (Fig. 4c-e). The XRD results also verified that
18 the original crystalline and amorphous phases present in the DM disappeared gradually, and that TiO₂
19 (P4₂/mnm [136]) was formed instead (Fig. 4f). There were some unidentified peaks found in the solid
20 residue but the amounts appeared insignificant compared with that of TiO₂. Remaining Nd-containing
21 phases were barely found in the solid residue at the leaching efficiency of 99%, also corroborating the

1 excellent leaching selectivity (Fig. S18).

2 We then precipitated Nd^{3+} with oxalic acid to recover Nd from the leachate as per the reaction:

3 $2\text{Nd}(\text{NO}_3)_3 + 3\text{H}_2\text{C}_2\text{O}_4 + x\text{H}_2\text{O} \rightarrow \text{Nd}_2(\text{C}_2\text{O}_4)_3 \cdot x\text{H}_2\text{O}(\text{s}) + 6\text{HNO}_3$. Guided by Hydra-Medusa simulation,

4 an excess amount of oxalate (ox) besides the stoichiometric amount is always required to achieve

5 complete Nd precipitation in a concentrated HNO_3 medium (Fig. S19a and b). The fraction of non-

6 precipitated Nd at the stoichiometric dosage, and the ratio of $[\text{ox}]/[\text{Nd}]$ for thorough precipitation both

7 decrease with an increase of initial Nd concentration (Fig. S19c and d). Therefore, the leachate

8 containing the highest Nd concentration from Run 5 (Table S3) was ideal to use as the feed solution for

9 Nd precipitation. The simulated dosage of oxalic acid for thorough precipitation ($[\text{ox}]/[\text{Nd}]=1.76$) was

10 verified experimentally to be more desirable than the stoichiometric dosage ($[\text{ox}]/[\text{Nd}]=1.5$), in terms

11 of the precipitation efficiency of both Nd and oxalate ions (Fig. 4g). Furthermore, HNO_3 could be

12 regenerated by the precipitation reaction (Fig. S20), which is an important factor since HNO_3 is more

13 expensive than more classic industrial acids. In theory, 100% HNO_3 should be recoverable from the

14 leaching solution with no change in total $[\text{HNO}_3]$ after the precipitation, but in reality, we measured a

15 recovery rate of 59.9%, with $[\text{HNO}_3]$ decreasing from 6.8 M to 6.3 M, due to HNO_3 thermal

16 decomposition and other side reactions.

17 Over the hydrometallurgical stage, the Nd recovery rate reached up to 98.2%, and the calcined

18 product at 900 °C showed a purity of Nd_2O_3 as high as 99.6% (Fig. 4h and Fig. S21), with an impurity

19 fraction composed of 0.3% ZnO and 0.1% CuO. By contrast, Nd recovery was impracticable for D&CM

20 when subjected to the same hydrometallurgical process (Fig. 4e and Fig. S22), due to the presence of

21 some impure metals like Cu, thus confirming the prerequisite role of beneficiation and pre-leaching to

22 the successful implementation of hydrometallurgy in the recycling route.

1 3.4. Leaching mechanism

2 The HNO₃ leaching step could be the most vulnerable step to the overall sustainability of this Nd
3 recycling route, as it is the only mineral acid-consuming step to tackle the corrosion resistive nature of
4 ceramics [52]. However, the Nd leaching efficiency and selectivity from the typical BaO-Nd₂O₃-TiO₂
5 system was unexpectedly high, enticing us to further investigate the leaching mechanism. According to
6 our leaching kinetic results, surface chemical control dominated the leaching reaction, thus aggressive
7 corrosion should occur at the solid-liquid interface. From the XRD results, intermediate phases were
8 not detected during the leaching although the layered perovskite-like BaO-Nd₂O₃-TiO₂ ceramics tend
9 to cleave along the (Ba_{1/2}O) plane [43]. The possible presence of Nd₂Ti₄O₁₁ was no exception because
10 it was deemed as the same phase as Nd₄Ti₉O₁₂ [53]. TiO₂ was found to be the dominant product in the
11 solid residue, which was verified by Hydra-Medusa simulation, as the dissociated TiO²⁺ can
12 progressively form TiO₂ crystals with the consumption of HNO₃ and increase of pH (Fig. S23).
13 According to Le Chatelier's principle, the crystallization phenomena could play a major driving role in
14 the leaching reaction by affecting its equilibrium, hence explaining the high leaching efficiency.
15 However, it still does not explain the leaching selectivity between Nd and Ba.

16 To elucidate the latter point, we explored the effect of bonding natures and leaching environments
17 through theoretical approaches. First, HNO₃ leaching results in material defects, have formation
18 energies which provide insights on their relative likelihood to be attacked [47]. To simplify computation,
19 the Nd/Ba vacancy model was established on Nd₂Ti₄O₁₁ and BaTi₂O₅ unit cells instead of the large
20 Ba_{3,6}Nd_{9,6}Ti₁₈O₅₄ unit cell (Fig. 5a). The defect formation energies (E_F) of Nd and Ba are 10.0 eV and
21 11.6 eV, respectively, based on the first-principle calculations, suggesting Nd could be more prone to
22 attack by acid than Ba. From a structural perspective, the BaO-Nd₂O₃-TiO₂ ceramic is constructed of a

1 network of corner-sharing TiO_6 octahedra, creating Nd-dominating tetragonal channels and Ba-
2 dominating pentagonal channels, thus Nd may be removed more easily when mutual diffusion occurs
3 between the ceramic ions with the acid medium [54]. On the other hand, we found that the Ba
4 concentrations in the leachate varied little with the increase of pulp density, which is reminiscent of the
5 effect of solubility. According to our solution simulation, NdNO_3^{2+} and $\text{Ba}(\text{NO}_3)_2$ are supposed to be
6 the major species for Nd and Ba in the given leaching environment (Fig. 5b). Although $\text{Ba}(\text{NO}_3)_2$ is
7 highly soluble in water, it has low solubility in concentrated HNO_3 (e.g. $\sim 10^{-3}$ M in 12 M HNO_3) unlike
8 the NdNO_3^{2+} ion [55], which is consistent with our results. Therefore, the concentrated HNO_3 leaching
9 environment appears crucial for enabling the Nd leaching selectivity.

10 Furthermore, we also examined the leaching reaction's thermodynamic data (see Table S4 and for
11 Table S5 thermodynamic data and the reaction considered, respectively). The cleavage reactions (1) and
12 (2) were validated not to occur spontaneously at 110 °C, as their values of $\Delta_r G^\circ$ are positive. The sub-
13 reactions (3)-(6) are thermodynamically favourable as their $\Delta_r G^\circ$ are all negative at 110 °C. The leaching
14 sub-reactions (3)-(5) are exothermic and the sub-reaction of TiO_2 formation is endothermic. Hence, the
15 overall major leaching exothermic reaction can be expressed as:

16 $\text{BaNd}_{5.3}\text{Ti}_{8.2}\text{O}_{25.35} + 17.9\text{H}^+ + 7.3\text{NO}_3^- \rightarrow 5.3\text{NdNO}_3^{2+} + \text{Ba}(\text{NO}_3)_2(\text{s}) + 8.2\text{TiO}_2(\text{s}) + 8.95\text{H}_2\text{O}$ (visualised
17 in Fig. 5c). Combining the estimated apparent activation energy ($E_a=51.5\pm 2.9$ kJ/mol) obtained from
18 Arrhenius equation plots (Fig. S24), we could roughly depict an energy diagram of the leaching reaction
19 (Fig. 5d), corroborating our observations on different effects of elevated temperatures on leaching rate
20 and leaching efficiency.

21 3.5. Features of the recycling flowsheet

22 The Nd recycling route developed in this study integrates many advantageous features that are

1 seldom present in existing e-waste recycling technologies. Firstly, the optical sorting is compatible with
2 high speed conveyor belts, it is a consistent and objective technique that identifies and sorts ECs by
3 geometric and visual criteria after their simultaneous disassembly. The ME-XRT sorting is element-
4 specific and is highly accurate even for complex EC structures. Compared with XRF technology, it
5 offers much better localization, although ME-XRT can be less sensitive in element inspection. The
6 combination of the optical and ME-XRT sorting aids in the development of an automated process,
7 favours both high efficiency and high accuracy, and avoids time-consuming and less efficient manual
8 or robotic picking. Secondly, in the beneficiation stage, it takes advantage of different physical
9 properties, including magnetism, density and fracture toughness, successively. Each processing unit is
10 simple to operate continuously without consuming exogenous material. This stage works as an
11 important link between the early sorting and the subsequent hydrometallurgy, so that the specific
12 element is further enriched and the chemical treatment is just pertinent to the ceramic fraction. Thirdly,
13 in the hydrometallurgy stage, as Nd is refined and pure for its use in dielectrics, the cumbersome solvent
14 extraction can be avoided by recovering pure Nd from the early element-specific sorting. Furthermore,
15 the chemicals used in this stage are arranged in a hyperlinked loop, partially eliminating HNO_3
16 consumption by regenerating it with more sustainable oxalic acid. All of the processing units can be up-
17 scaled to industrial equipment from a flowsheet projection view (Fig. 6a). The three stages are flexible
18 enough to be either operated in different companies or integrated together into one company.

19 *3.6. Economic assessment*

20 To further study the potential of this technically feasible process, we evaluated the economic
21 viability of this new Nd recycling route by industrial process simulation. First, mass and energy were
22 balanced separately for the upstream sorting and beneficiation process (Fig. S25) and the downstream

1 hydrometallurgy process (Fig. S26) according to the weight percentage, stoichiometry and operating
2 conditions obtained from our lab-scale work. Then we defined the price of all the input and output
3 materials based on current market prices from various sources (Table S6). The detailed cost and benefit
4 analysis is shown in Table S7. The payback time is 3.6 and 4.2 years, for the upstream and downstream
5 sub-processes respectively (Fig. 6b and c). However, this is a conservative scenario as we have not yet
6 considered the recovery of other metals (eg. Cu, Ag and Sn) that are already known to be economically
7 viable throughout classical processing. With these estimates, we concluded that the Nd recycling
8 process is profitable, hence we are currently scaling it up in our facility.

9 **4. Conclusions**

10 In summary, our study proves that, for the first time, one can profitably recycle Nd from the ceramic
11 fraction contained in highly complex e-wastes following a technically, economically and
12 environmentally feasible route. In virtue of simultaneous disassembly, optical and MEXRT sorting, the
13 issue of high Nd dilution in e-wastes can be effectively tackled, while other valuable ECs can be
14 streamed into different categories with this element-specific sorting. The employment of physical
15 beneficiation can further reduce the complexity of elemental composition by taking advantage of
16 different physical properties. Owing to the aforementioned processes, the obtained Nd concentrates
17 (BaO-Nd₂O₃-TiO₂ dielectric materials) are merely subject to simple leaching and precipitation methods,
18 to fulfil Nd recycling with high selectivity. Besides, nearly 60% HNO₃ can be regenerated by more
19 sustainable H₂C₂O₄ in each loop of processing. This integrated Nd recycling route leads to a high
20 recovery efficiency (91.1%) and a high purity of neodymium oxide product (>99.6%). To further extend
21 the recycling potential, future studies will investigate recycling Nd-doped dielectrics, which contain
22 less Nd, more miniaturized MLCCs and other REEs. More broadly, our research shows a promising

1 prospect for urban-mining other, yet unrecycled, “specialty metals” from e-wastes in an economically
2 and environmentally favourable way.

3

4 **Declaration of Competing Interest**

5 All authors Competing interests: JCG and AB wish to declare that ME-XRT detector ME100 used
6 in the work described here is commercialised by Detection Technology under patent licensing from
7 CEA. The authors declare no other competing interests.

8

9 **Acknowledgements**

10 All authors acknowledge financial support from SCARCE project, which is supported by the
11 National Research Foundation, Prime Minister’s Office, Singapore, the Ministry of National Develop-
12 ment, Singapore, and National Environment Agency, Ministry of the Environment and Water Resource,
13 Singapore under the Closing the Waste Loop R&D Initiative as part of the Urban Solutions &
14 Sustainability – Integration Fund [Award No. USS-IF-2018-4]. XD acknowledges Dr. Varun Rai for
15 assistance on ICP-OES measurements, Xianyi Tan and Lan Yang for XRD and SEM-EDS
16 characterizations, and Dr. Wenjing Huang for IC analysis.

17

18 **References**

- 19 [1] T. Cheisson, E.J. Schelter, Rare earth elements: Mendeleev’s bane, modern marvels, *Science* 363 (2019) 489-
20 493, <https://www.science.org/doi/10.1126/science.aau7628>.
- 21 [2] T. Zhong, J.M. Kindem, J.G. Bartholomew, J. Rochman, I. Craiciu, E. Miyazono, M. Bettinelli, E. Cavalli, V.
22 Verma, S.W. Nam, Nanophotonic rare-earth quantum memory with optically controlled retrieval, *Science* 357
23 (2017) 1392-1395, <https://www.science.org/doi/abs/10.1126/science.aan5959>.
- 24 [3] R. Ryoo, J. Kim, C. Jo, S.W. Han, J.-C. Kim, H. Park, J. Han, H.S. Shin, J.W. Shin, Rare-earth–platinum alloy
25 nanoparticles in mesoporous zeolite for catalysis, *Nature* 585 (2020) 221-224, [https://doi.org/10.1038/s41586-](https://doi.org/10.1038/s41586-020-2671-4)
26 020-2671-4.

- 1 [4] H. Wang, X. Wu, Y. Yang, M. Nishiura, Z. Hou, Co - syndiospecific Alternating Copolymerization of
2 Functionalized Propylenes and Styrene by Rare - Earth Catalysts, *Angew. Chem. Int. Ed.* 132 (2020) 7240-7244,
3 <https://doi.org/10.1002/anie.201915760>.
- 4 [5] The State Council Information Office of the People's Republic of China, *Situation and Policies of China's Rare*
5 *Earth Industry*, Beijing, 2010.
- 6 [6] U.S. Government Accountability Office, *Rare earth materials in the defense supply chain*, Washington, D.C.,
7 2010.
- 8 [7] European Commission, *Critical raw materials for the EU. Report of the Ad-hoc Working Group on Defining*
9 *Critical Raw Materials*, Brussels, Belgium, 2018.
- 10 [8] Global Industry Analysts Inc, *Rare Earth Elements - Global Market Trajectory & Analytics*, 2021.
- 11 [9] U.S. Department of Energy, *Critical materials strategy*, 2010.
- 12 [10] E. Alonso, A.M. Sherman, T.J. Wallington, M.P. Everson, F.R. Field, R. Roth, R.E. Kirchain, Evaluating rare
13 earth element availability: A case with revolutionary demand from clean technologies, *Environ. Sci. Technol.* 46
14 (2012) 3406-3414, <https://doi.org/10.1021/es203518d>.
- 15 [11] J.C. Lee, Z. Wen, Pathways for greening the supply of rare earth elements in China, *Nature Sustainability* 1
16 (2018) 598-605, <https://doi.org/10.1038/s41893-018-0154-5>.
- 17 [12] Y. Law, Politics could upend global trade in rare earth elements, *Science* 364 (2019) 114-115,
18 <https://www.science.org/doi/full/10.1126/science.364.6436.114>.
- 19 [13] A. El Maangar, J. Theisen, C. Penisson, T. Zemb, J.-C.P. Gabriel, A microfluidic study of synergic liquid–liquid
20 extraction of rare earth elements, *Phys. Chem. Chem. Phys.* 22 (2020) 5449-5462,
21 <https://doi.org/10.1039/C9CP06569E>.
- 22 [14] K. Binnemans, P.T. Jones, B. Blanpain, T. Van Gerven, Y. Yang, A. Walton, M. Buchert, Recycling of rare
23 earths: a critical review, *J. Clean. Prod.* 51 (2013) 1-22, <https://doi.org/10.1016/j.jclepro.2012.12.037>.
- 24 [15] P. Froehlich, T. Lorenz, G. Martin, B. Brett, M. Bertau, Valuable metals—recovery processes, current trends,
25 and recycling strategies, *Angew. Chem. Int. Ed.* 56 (2017) 2544-2580, Valuable metals—recovery processes,
26 current trends, and recycling strategies.
- 27 [16] K.K. Yadav, M. Anitha, D. Singh, V. Kain, NdFeB magnet recycling: Dysprosium recovery by non-dispersive
28 solvent extraction employing hollow fibre membrane contactor, *Sep. Purif. Technol.* 194 (2018) 265-271,
29 <https://doi.org/10.1016/j.seppur.2017.11.025>.
- 30 [17] A. Kumari, M.K. Sinha, S. Pramanik, S.K. Sahu, Recovery of rare earths from spent NdFeB magnets of wind
31 turbine: Leaching and kinetic aspects, *Waste Manage.* 75 (2018) 486-498,
32 <https://doi.org/10.1016/j.wasman.2018.01.033>.
- 33 [18] H.D. Bandara, K.D. Field, M.H. Emmert, Rare earth recovery from end-of-life motors employing green
34 chemistry design principles, *Green Chem.* 18 (2016) 753-759, <https://doi.org/10.1039/C5GC01255D>.
- 35 [19] Y. Yao, N.F. Farac, G. Azimi, Supercritical fluid extraction of rare earth elements from nickel metal hydride
36 battery, *ACS Sustain. Chem. Eng.* 6 (2018) 1417-1426, <https://doi.org/10.1021/acssuschemeng.7b03803>.
- 37 [20] X. Yang, J. Zhang, X. Fang, Rare earth element recycling from waste nickel-metal hydride batteries, *J.*
38 *Hazard. Mater.* 279 (2014) 384-388, <https://doi.org/10.1016/j.jhazmat.2014.07.027>.
- 39 [21] A. Maurice, J. Theisen, J.-C.P. Gabriel, Microfluidic lab-on-chip advances for liquid–liquid extraction process
40 studies, *Curr. Opin. Colloid Interface Sci.* 46 (2020) 20-35, <https://doi.org/10.1016/j.cocis.2020.03.001>.
- 41 [22] A.A. Maurice, J. Theisen, V. Rai, F. Olivier, A. El Maangar, J. Duhamet, T. Zemb, J.C.P. Gabriel, First online X-
42 ray fluorescence characterization of liquid-liquid extraction in microfluidics, *Nano Select* (2021),
43 <https://doi.org/10.1002/nano.202100133>.
- 44 [23] A.M. Schmitz, B. Pian, S. Medin, M.C. Reid, M. Wu, E. Gazel, B. Barstow, Generation of a *Gluconobacter*

1 oxydans knockout collection for improved extraction of rare earth elements, *Nat. Commun.* 12 (2021) 1-11,
2 <https://doi.org/10.1038/s41467-021-27047-4>.

3 [24] S. Dev, A. Sachan, F. Dehghani, T. Ghosh, B.R. Briggs, S. Aggarwal, Mechanisms of biological recovery of
4 rare-earth elements from industrial and electronic wastes: A review, *Chem. Eng. J.* 397 (2020) 124596,
5 <https://doi.org/10.1016/j.cej.2020.124596>.

6 [25] T. Hatanaka, A. Matsugami, T. Nonaka, H. Takagi, F. Hayashi, T. Tani, N. Ishida, Rationally designed
7 mineralization for selective recovery of the rare earth elements, *Nat. Commun.* 8 (2017) 1-10,
8 <https://doi.org/10.1038/ncomms15670>.

9 [26] H. Yang, F. Peng, D.E. Schier, S.A. Markotic, X. Zhao, A.N. Hong, Y. Wang, P. Feng, X. Bu, Selective
10 Crystallization of Rare - Earth Ions into Cationic Metal - Organic Frameworks for Rare - Earth Separation,
11 *Angew. Chem. Int. Ed.* 60 (2021) 11148-11152, <https://doi.org/10.1002/anie.202017042>.

12 [27] P. Wamea, M.L. Pitcher, J. Muthami, A. Sheikhi, Nanoengineering cellulose for the selective removal of
13 neodymium: Towards sustainable rare earth element recovery, *Chem. Eng. J.* 428 (2022) 131086,
14 <https://doi.org/10.1016/j.cej.2021.131086>.

15 [28] J.A. Bogart, C.A. Lippincott, P.J. Carroll, E.J. Schelter, An Operationally Simple Method for Separating the
16 Rare - Earth Elements Neodymium and Dysprosium, *Angew. Chem. Int. Ed.* 127 (2015) 8340-8343,
17 <https://doi.org/10.1002/ange.201501659>.

18 [29] H. Fang, B.E. Cole, Y. Qiao, J.A. Bogart, T. Cheisson, B.C. Manor, P.J. Carroll, E.J. Schelter, Electro - kinetic
19 Separation of Rare Earth Elements Using a Redox - Active Ligand, *Angew. Chem. Int. Ed.* 129 (2017) 13635-
20 13639, <https://doi.org/10.1002/ange.201706894>.

21 [30] European Commission, Report on critical raw materials and the circular economy, Brussels, Belgium, 2018.

22 [31] T.G. Goonan, Rare earth elements: End use and recyclability, US Department of the Interior, US Geological
23 Survey, 2011.

24 [32] W. Wersing, Microwave ceramics for resonators and filters, *Curr. Opin. Solid State Mater. Sci.* 1 (1996) 715-
25 731, [https://doi.org/10.1016/S1359-0286\(96\)80056-8](https://doi.org/10.1016/S1359-0286(96)80056-8).

26 [33] M.A. Alam, L. Zuga, M.G. Pecht, Economics of rare earth elements in ceramic capacitors, *Ceram. Int.* 38
27 (2012) 6091-6098, <https://doi.org/10.1016/j.ceramint.2012.05.068>.

28 [34] G. Wang, Q. Fu, P. Guo, M. Hu, H. Wang, S. Yu, Z. Zheng, W. Luo, Crystal structure, spectra analysis and
29 dielectric characteristics of Ba₄M₂₈/3Ti₁₈O₅₄ (M= La, Pr, Nd, and Sm) microwave ceramics, *Ceram. Int.* 47
30 (2021) 1750-1757, <https://doi.org/10.1016/j.ceramint.2020.08.294>.

31 [35] A.K. Awasthi, J. Li, L. Koh, O.A. Ogunseitan, Circular economy and electronic waste, *Nature Electronics* 2
32 (2019) 86-89, <https://doi.org/10.1038/s41928-019-0225-2>.

33 [36] A.A. Maurice, K.N. Dinh, N.M. Charpentier, A. Brambilla, J.-C.P. Gabriel, Dismantling of Printed Circuit
34 Boards Enabling Electronic Components Sorting and Their Subsequent Treatment Open Improved Elemental
35 Sustainability Opportunities, *Sustainability* 13 (2021) 10357, <https://doi.org/10.3390/su131810357>.

36 [37] Y. Lu, B. Yang, Y. Gao, Z. Xu, An automatic sorting system for electronic components detached from waste
37 printed circuit boards, *Waste Manage.* 137 (2022) 1-8, <https://doi.org/10.1016/j.wasman.2021.10.016>.

38 [38] Q. Zeng, J.-B. Sirven, J.-C.P. Gabriel, C.Y. Tay, J.-M. Lee, Laser induced breakdown spectroscopy for plastic
39 analysis, *TrAC, Trends Anal. Chem.* (2021) 116280, <https://doi.org/10.1016/j.trac.2021.116280>.

40 [39] A. Sakdinawat, D. Attwood, Nanoscale X-ray imaging, *Nature photonics* 4 (2010) 840-848,
41 <https://doi.org/10.1038/nphoton.2010.267>.

42 [40] K.C. Liddell, Shrinking core models in hydrometallurgy: What students are not being told about the
43 pseudo-steady approximation, *Hydrometallurgy* 79 (2005) 62-68,
44 <https://doi.org/10.1016/j.hydromet.2003.07.011>.

- 1 [41] Y. Ziouane, G. Leturcq, New modeling of nitric acid dissociation function of acidity and temperature, ACS
2 omega 3 (2018) 6566-6576, <https://doi.org/10.1021/acsomega.8b00302>.
- 3 [42] A. Nastic, A. Merati, M. Bielawski, M. Bolduc, O. Fakolujo, M. Nganbe, Instrumented and Vickers
4 indentation for the characterization of stiffness, hardness and toughness of zirconia toughened Al₂O₃ and SiC
5 armor, J. Mater. Sci. Technol. 31 (2015) 773-783, <https://doi.org/10.1016/j.jmst.2015.06.005>.
- 6 [43] X. Kuang, F. Liao, S. Tian, X. Jing, A powder X-ray diffraction refinement of the BaNd₂Ti₃O₁₀ structure,
7 Mater. Res. Bull. 37 (2002) 1755-1761, [https://doi.org/10.1016/S0025-5408\(02\)00856-5](https://doi.org/10.1016/S0025-5408(02)00856-5).
- 8 [44] M. Segall, P.J. Lindan, M.a. Probert, C.J. Pickard, P.J. Hasnip, S. Clark, M. Payne, First-principles simulation:
9 ideas, illustrations and the CASTEP code, J. Phys.: Condens. Matter 14 (2002) 2717.
- 10 [45] J.P. Perdew, K. Burke, M. Ernzerhof, Generalized gradient approximation made simple, Phys. Rev. Lett. 77
11 (1996) 3865, <https://doi.org/10.1103/PhysRevLett.77.3865>.
- 12 [46] D. Vanderbilt, Soft self-consistent pseudopotentials in a generalized eigenvalue formalism, Physical review
13 B 41 (1990) 7892, <https://doi.org/10.1103/PhysRevB.41.7892>.
- 14 [47] W. Zhang, Z. Xu, H. Wang, First-Principles Study of the Native Defects in In I Crystal, J. Acta Physica Sinica
15 62 (2013) 243101.
- 16 [48] J. Kołacz, A. Wieniewski, Advanced separation methods in the X-ray-optical sorting systems, CUPRUM–
17 Czasopismo Naukowo-Techniczne Górnictwa Rud (2015) 75.
- 18 [49] A. Brambilla, A. Gorecki, A. Potop, Characterizing a sample by material basis decomposition, United
19 States Patent, Google Patents, U.S., 2021.
- 20 [50] L. Zhang, X. Chen, N. Qin, X. Liu, Upper limit of x in Ba₆–3xNd₈+2xTi₁₈O₅₄ new tungsten bronze solid
21 solution, J. Eur. Ceram. Soc. 27 (2007) 3011-3016, <https://doi.org/10.1016/j.jeurceramsoc.2007.01.007>.
- 22 [51] P. Meshram, B. Pandey, T. Mankhand, Hydrometallurgical processing of spent lithium ion batteries (LIBs) in
23 the presence of a reducing agent with emphasis on kinetics of leaching, Chem. Eng. J. 281 (2015) 418-427,
24 <https://doi.org/10.1016/j.cej.2015.06.071>.
- 25 [52] S.M. Lee, W.B. Lim, Y.S. Cho, Corrosion behavior of highly-crystallizable BaO–Nd₂O₃–TiO₂–B₂O₃ glass-
26 based composites, Corros. Sci. 66 (2013) 399-403, <https://doi.org/10.1016/j.corsci.2012.08.062>.
- 27 [53] W. Gong, R. Zhang, Phase relationship in the TiO₂–Nd₂O₃ pseudo-binary system, J. Alloys Compd. 548
28 (2013) 216-221, <https://doi.org/10.1016/j.jallcom.2012.08.112>.
- 29 [54] F. Azough, R.J. Cernik, B. Schaffer, D. Kepaptsoglou, Q.M. Ramasse, M. Bigatti, A. Ali, I. MacLaren, J. Barthel,
30 M. Molinari, Tungsten Bronze Barium Neodymium Titanate (Ba₆–3 n Nd₈+ 2 n Ti₁₈O₅₄): An Intrinsic
31 Nanostructured Material and Its Defect Distribution, Inorg. Chem. 55 (2016) 3338-3350,
32 <https://doi.org/10.1021/acs.inorgchem.5b02594>.
- 33 [55] P. Butkalyuk, I. Butkalyuk, R. Kuznetsov, A. Kupriyanov, R. Abdullov, Solubility of Radium Nitrate in Nitric
34 Acid Solutions, Radiochemistry 61 (2019) 12-17, <https://doi.org/10.1134/S106636221901003X>.

1 **Figure captions**

2

3 **Fig. 1.** Integrated route of Nd recycling from waste PCBs.

4 **Fig. 2.** Sorting performance of ECs. a) 3D schematic illustration of our optical prototype for sorting of various
5 ECs. The inset images indicate the pictures of various ECs captured by the camera; b) Recovery rate confusion
6 matrix of sorted ECs in the size category of 5-10 mm; c) Accuracy confusion matrix of sorted ECs in the size
7 category of 5-10 mm; d) Schematic principle of ME-XRT acquisition in which the sample is scanned along the
8 long axis using a fan X-ray beam (for magnification); e) ME-XRT transmittance mapping image of optically
9 sorted SLCCs; f) Representative ME-XRT spectra for three different types of SLCCs, including Ba-containing
10 but Nd-free (Ba), Nd-containing (Nd) and Ta-containing (Ta) SLCCs. The dashed lines indicate the detected
11 minima of the curves and the half-transparent rectangles indicate the K-edges of Ba, Nd and Ta in a range of ± 2 ,
12 ± 2 and ± 5 keV, respectively.

13 **Fig. 3.** Precise beneficiation of SLCCs. a) Flow chart of physical beneficiation process and associated mass
14 fraction of materials. b) Element compositions of Nd concentrates and Nd recovery rate in each step.

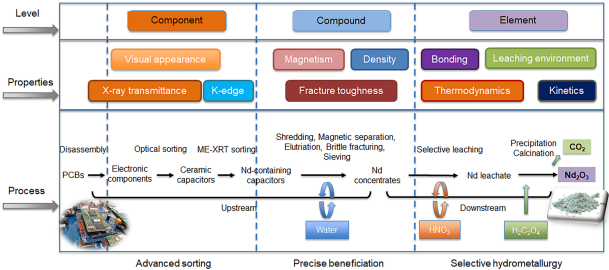
15 **Fig. 4.** Nd recovery by selective hydrometallurgy. a) Comparison of three mineral acids on the selectivity of
16 leaching at 70 °C and a pulp density of 50 g/L for 80 h. b) Nd leaching kinetic curve at the optimized leaching
17 condition (10 M HNO₃, 110 °C, 400 g/L), presented as Nd concentration and leaching efficiency versus time. c)
18 SEM image of original DM. d) SEM image of solid residue after leaching of DM for 86 h in the batch of Run 15.
19 e) SEM image of solid residue after leaching of DM for 28 h in the batch of Run 5. f) XRD pattern of DM and
20 solid residue after the leaching of DM at various leaching efficiency. g) Precipitation efficiency of Nd and oxalate
21 at a ratio of [ox]/[Nd] required by a stoichiometric dosage and a simulated excess dosage. h) Comparison of DM

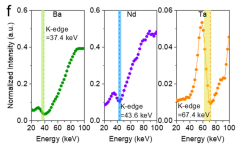
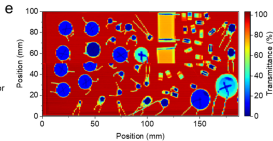
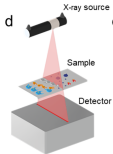
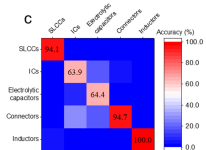
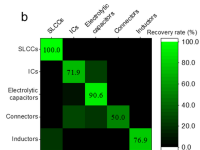
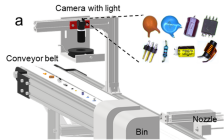
1 and D&CM as precursors subject to the same hydrometallurgical process in terms of Nd recovery rate and product
2 purity.

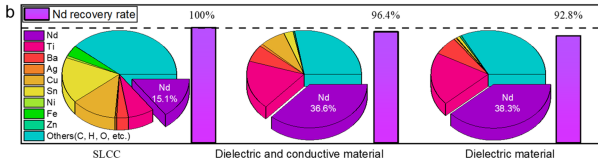
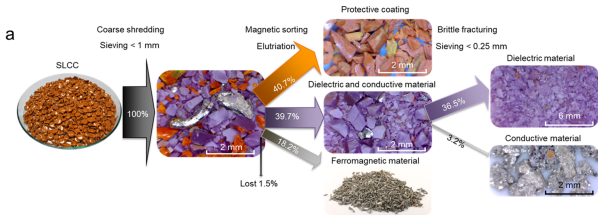
3 **Fig. 5.** Proposed mechanism on leaching selectivity. a) Simulated Nd/Ba vacancy model by removing one Nd/Ba
4 atom from $\text{Nd}_2\text{Ti}_4\text{O}_{11}/\text{BaTi}_2\text{O}_5$ unit cell and the resulting defect formation energy. b) Simulated fractions of Nd
5 and Ba species in the leachate versus the change of pH, when $[\text{Nd}^{3+}]_{\text{total}} = 962 \text{ mM}$, $[\text{TiO}^{2+}]_{\text{total}} = 14.2 \text{ Mm}$,
6 $[\text{Ba}^{2+}]_{\text{total}} = 173 \text{ mM}$ and $[\text{NO}_3^-]_{\text{total}} = 10.0 \text{ M}$. c) Energy diagram of the Nd leaching reaction from DM with 10 M
7 HNO_3 at 110 °C. d) Proposed reaction mechanism of selective Nd leaching from DM.

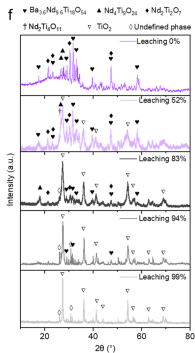
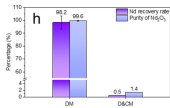
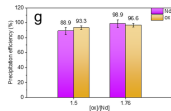
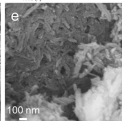
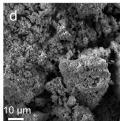
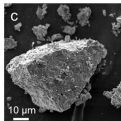
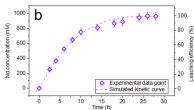
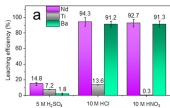
8 **Fig. 6.** Flowsheet and economic assessment of the Nd recycling route. a) Conceived flowsheet of the Nd recycling
9 route (generated using HSC Chemistry software). b) Cost and benefit analysis of the sorting and beneficiation
10 section over 10 years. c) Cost and benefit analysis of the hydrometallurgy section over 10 years.

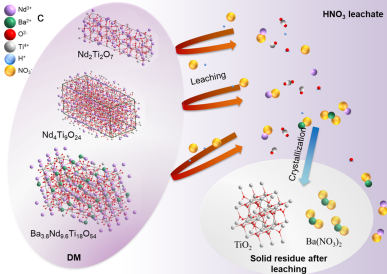
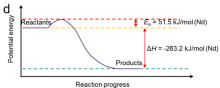
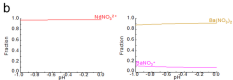
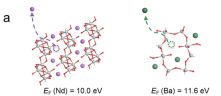
11





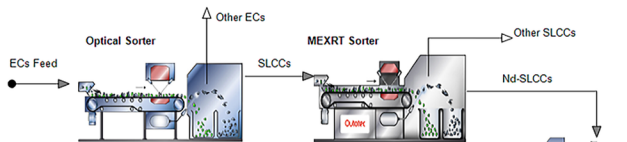




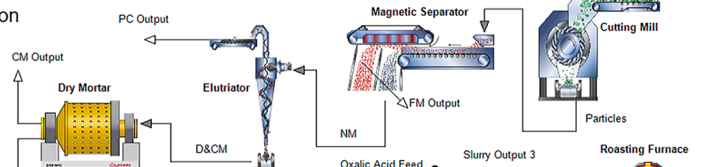


a

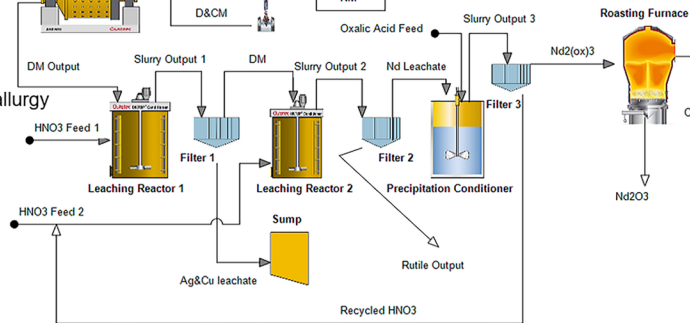
Sorting



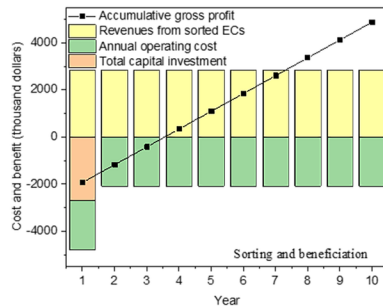
Beneficiation



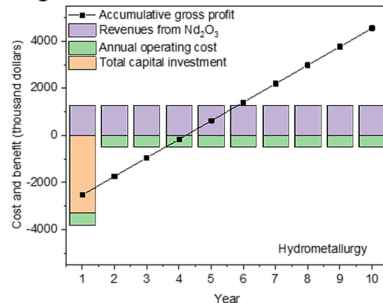
Hydrometallurgy



b



c



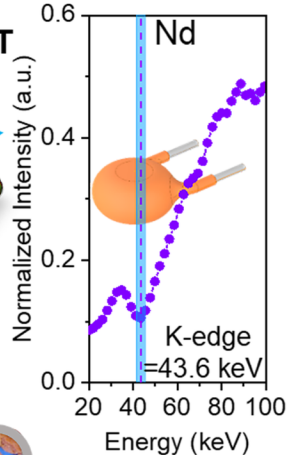
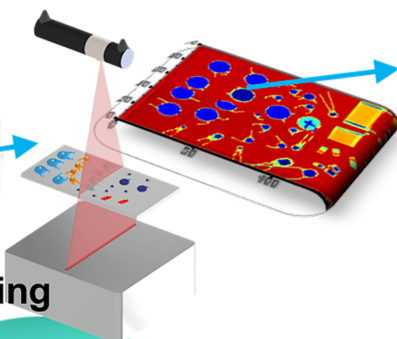
A Needle in a Haystack



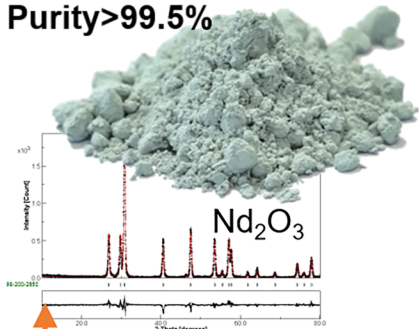
Machine vision

Sorting

Multi-energy XRT

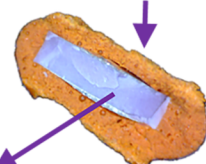


Purity > 99.5%



High selectivity

Recovery efficiency = 91%



Beneficiation

